LES study of breakdown control of A-pillar vortex

S. Krajnović and J. Östh
Department of Applied Mechanics, Chalmers University of Technology, Gothenburg, Sweden
B. Basara
AST-AVL, Graz, Austria
[Received date; Accepted date] – to be inserted later

Abstract
Active flow control of the longitudinal vortices that developed near and around simplified A-pillar of a generic vehicle was studied using large eddy simulation (LES). The LES results were validated against existing Particle Image Velocimetry (PIV) and aerodynamic drag data. The LES results were further used to study the flow physics responsible for the development of longitudinal vortices, in particular the vortex breakdown process. Tangential blowing and suction into the shear layer rolling into the longitudinal vortices was found to be a sensitive process that can cause instabilities in the flow. The resulting LES flows also show that actuation influences not only the longitudinal vortex nearest to the actuation slot but also the overall flow. Thus, the influence of the flow control actuation on the entire flow must be considered in order to be able to find the appropriate level of control for optimal aerodynamic performance.

1. INTRODUCTION
The separated flow around ground vehicles consists of two types of separations [1]. The first type sometimes denoted quasi-two-dimensional occurs at an edge that is nearly orthogonal with respect to the direction of the flow. Examples of such separation regions are on the front of the hood, in front of the windshields and at the truncated rear surface of the vehicle resulting in the wake. Flow physics of these structures is studied in [2] and their control in [3].

The separation at edges around which air flows at an angle belongs to the second type, sometimes called three-dimensional (although it should be recognized that all types of separations around ground vehicles are truly three-dimensional). Examples of such a separation occur around the front pillar (A-pillar) and back pillar (C-pillar) of cars, resulting in longitudinal cone-shaped streamwise vortices. These vortices are rich in energy and are responsible for a large portion of the total aerodynamic drag (they are sometimes denoted "drag inducing vortices"). The level of vorticity in the separated shear layer that rolls in these longitudinal vortices is dependent on several geometrical conditions, of which the inclination of the edge at which they separate from the body is most important. The stronger of the two pillar vortices is that around the C-pillar formed at the slanted back of a car, and has been studied extensively around the generic vehicle called the Ahmed body [4-5]. The formation and control of the longitudinal vortices around the C-pillar are similar to those around the A-pillar but there are also differences. Despite the similarities between the two types of longitudinal vortices, the present manuscript will deal only with the A-pillar vortices. For an understanding of the flow physics of C-pillar vortices and their control we refer to Krajnovic and Davidson [4-5] and Krajnovic et al. [6-7].

The trailing vortices formed around A-pillars have an influence on both the aerodynamics and the aero-acoustics of passenger vehicles. According to a recent study by Alam et al. [8], the flow around the A-pillar is the main source of "in-cabin" aero-acoustic noise. The reason for the generation of aero-acoustic noise from the trailing vortex around the A-pillar can be found in fluctuating pressure on the surface of the car. Unsteady wall pressure field around the A-pillar was studied by Hoarau et al. [9], de Moraes et al. [10] and Levy et al. [11]. While distinct frequency peaks were found in pressure signals in [9-10], a broadband power spectrum resulted from the pressure signal in [11].

The swirling velocity of the A-pillar longitudinal vortices induces local total pressure losses that contribute to aerodynamic drag [12]. An estimate of the contribution of the A-pillars vortices to aerodynamic drag of some 10% for a three-box passenger car was reported by Hucho [1]. Thus, an

understanding of the development of these structures and their control could lead to a significant reduction in drag.

An alternative to the classical definition of drag as a combination of pressure drag and friction drag integrated over the surface of a vehicle was presented by Onorato et al. [12]. According to [12], the aerodynamic drag can be defined by an integral evaluation of the momentum around the car according to the equation:

$$F_x \int_A (P_{io} - P_1) d\sigma + \frac{\rho V_0^2}{2} \int_A \left(\frac{U_Y^2}{V_0^2} - \frac{U_Z^2}{V_0^2} \right) d\sigma - \frac{\rho V_0^2}{2} \int_A \left(1 - \frac{U_X}{V_0} \right)^2 d\sigma \quad (1)$$

The first term in the equation is the total pressure loss in the vehicle wake. The second term represents the rotational kinetic energy that is partly dissipated in the longitudinal vortices such as those around A-pillar. The last term is the longitudinal velocity deficit in the wake. Thus, a reduction in aerodynamic drag can be achieved by a reduction of the wake width A, by reducing the total pressure loss between the front and rear of the vehicle and by reducing the swirling intensity of the three-dimensional flow structures. The present work aims to explore the flow physics responsible for one contributor to the second term in Eq. 1.

Finally, it is worth mentioning that A-pillar longitudinal vortices have an influence on aerodynamic effects other than drag. For example, water distribution and dirt deposition on the vehicle's lateral windows are influenced by these flow structures. Furthermore, lateral stability, in particular in overtaking and passing situations, is influenced by these flow features.

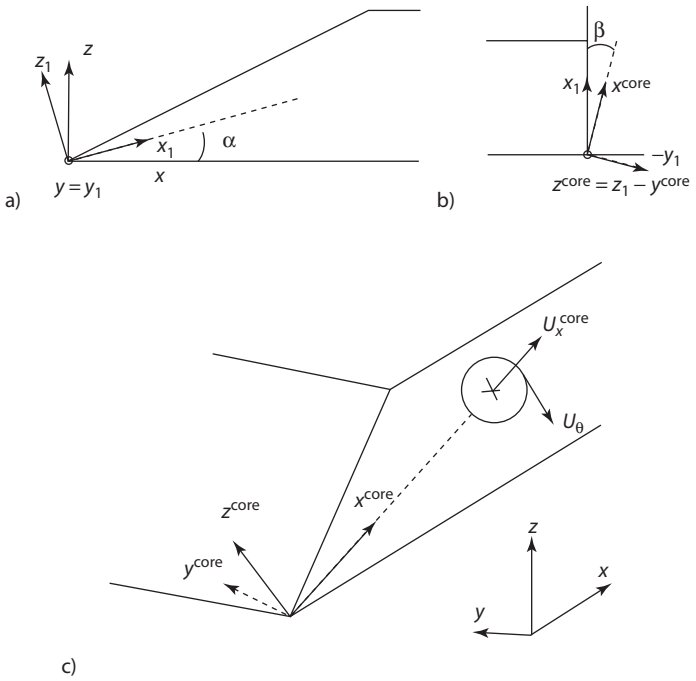

Figure 1. Definition of the coordinate system aligned with the vortex core. a) Side view showing first rotation of angle α, b) View from above showing second rotation of angle β, c) Comparison of the final coordinate system (x^{core}, y^{core}, z^{core}) with the original one (x, y, z).

Other vehicles that are influenced by A-pillar vortices are trains, in particular high-speed trains which have lateral edges of the front inclined at some angle with respect to the direction of the flow. Here, these vortices are particularly important for the lateral stability of trains under the influence of crosswinds and are the subject of febrile research [13-14].

2. DEFINITION OF THE COORDINATE SYSTEM

Analysis of the flow in and around the inclined longitudinal vortices requires introduction of a new coordinate system (x^{core}, y^{core}, z^{core}) where axis x^{core} is aligned with the core of the trailing vortex. This coordinate system is defined on the basis of the initial coordinate system (x, y, z) by performing two

rotations as shown in Fig. 1. The first rotation of angle α around the axis y transforms the initial coordinate system (x, y, z) into (x_1, y_1, z_1) shown in Fig. 1a. A second rotation of angle β around the z_1 axis transforms (x_1, y_1, z_1) into $(x^{core}, y^{core}, z^{core})$ as shown in Fig. 1b. Angles α and β are computed from the vortex core of the trailing vortex (this will be demonstrated later in the article). The resulting coordinate system $(x^{core}, y^{core}, z^{core})$ together with the azimuthal velocity component U_θ and an axial component U_x^{core}, that are defined by this coordinate system, are presented in Fig. 1c.

3. VORTEX BREAKDOWN OF LONGITUDINAL VORTEX

The longitudinal vortices formed around the A-pillar are characterized by a strong swirl (azimuthal) velocity component and an axial component that changes in strength from large to small giving the longitudinal vortex a jet-like to wake-like character, respectively. At some distance from the leading edge of the body the longitudinal vortices experience a sudden disorganization known as vortex breakdown which can be characterized by a rapid deceleration of both the axial and swirl components of the velocity and a sudden expansion of the vortex core. This phenomenon was first observed in experiments with a slender delta wing [15] but is known to exist in similar applications such as the A-pillar of vehicles. It is known from previous work that during the breakdown, the axial velocity component rapidly decreases until it reaches a stagnation point or becomes negative on the vortex axis. The stagnation point is called the breakdown location, it is unsteady and it oscillates about some mean position along the axis of vortex core [16]

Two parameters are important for the occurrence and movement of vortex breakdown, swirl level and pressure gradient affecting the vortex core. An increase in the magnitude of either parameter promotes earlier breakdown. An experimental study of delta wings [17] shows that vortex breakdown moves upstream over the delta wing when the magnitude of either parameter is increased. The method used in the present work to promote or delay vortex breakdown is to increase/decrease swirl by adding/removing momentum in the shear layer.

Since the vorticity of the longitudinal vortices originates from the separation line along the lateral leading edge, the strength and, location of lateral vortices as well as their vortex breakdown can be influenced by controlling the properties of the shear layer involved in their formation. The present work follows the experimental work of Lehugeur et al. [18] where steady tangential blowing or steady suction at the leading edge were used to control the properties of the shear layer and the swirl level of the longitudinal vortices. The two actuation methods, blowing and suction, differ in the way they influence the shear layers. Tangential blowing adds the vorticity and thus increases the swirl level and the strength of the longitudinal vortex. Tangential suction on the other hand reduces the vorticity and weakens the trailing vortex.

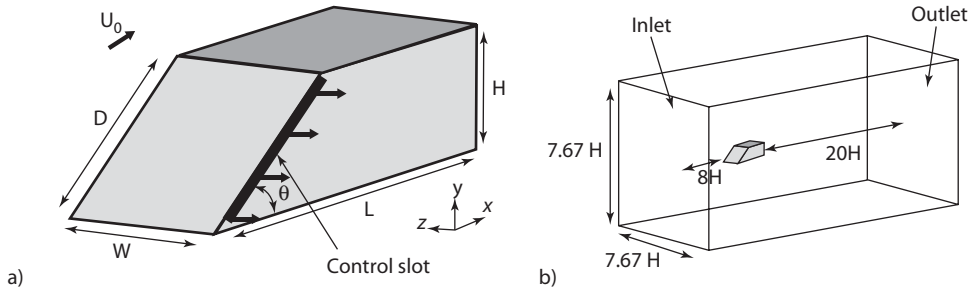

Figure 2. a) Geometry of the generic vehicle body. b) Computational domain.

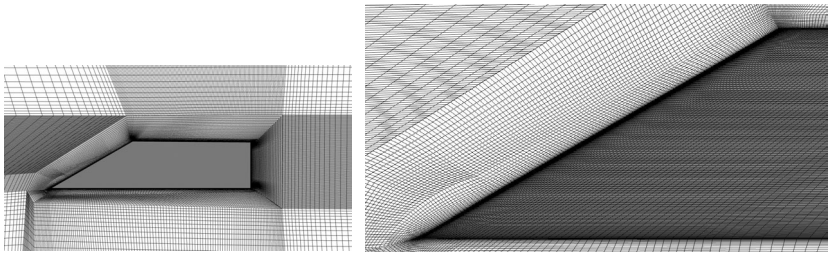

a) b)

Figure 3. a) Computational grid from the case with flow control. b) Zoom of the front of the body with surface grid.

4. DESCRIPTION OF THE MODEL

The geometry of the dihedral bluff body used in the LES simulations to control the A-pillar vortex is presented in Fig. 2a. The edges of the model are all sharp. The length, L, of the model is 0.17 m. The height, H, and width, W, are equal to H/L = 0.23 and W/L = 0.3, respectively. The windscreen makes an angle $\theta = 30°$ with the bottom surface of the model. The length of the windscreen, D, is equal to D/L = 0.47. The axes of the coordinate system are directed as shown in Fig. 2a. The x-axis corresponds to the streamwise direction, the z-axis to the transversal direction and the y-axis to the spanwise direction of the flow. The actuation is applied on one side of the model only (Fig. 2a). The control slot is located along the left side of the windscreen and length λ and width e of the slot are $\lambda/D = 0.95$ and e/D = 0.005, respectively. All dimensions of the geometry used in the present LES simulations are the same as those used in the experiments by Lehugeur et al. [18]. The model was mounted on an egg-shaped section support in the experiments that held it in the center of the working section of the wind tunnel. The support is not included in the geometry used in the present LES simulations as its influence on the longitudinal A-pillar vortex is expected to be minimal. The Reynolds number based on the inlet velocity and the model length is $\mathrm{Re}=8.5 \times 10^4$, the same as in the experiment [18].

5. NUMERICAL DETAILS

The governing LES equations are the incompressible Navier-Stokes and the continuity equations filtered with the implicit spatial filter of characteristic width Δ (Δ is the grid resolution in this work):

$$\frac{\partial \overline{u}_i}{\partial t} + \frac{\partial}{\partial x_j}(\overline{u}_i \overline{u}_j) = -\frac{1}{\rho}\frac{\partial \overline{p}}{\partial x_i} + \nu \frac{\partial^2 \overline{u}_i}{\partial x_i \partial x_j} - \frac{\partial \tau_{ij}}{\partial x_j} \tag{2}$$

and

$$\frac{\partial \overline{u}_i}{\partial x_i} = 0 \tag{3}$$

Here, $\overline{u}_i$ and $\overline{p}_i$ are the resolved velocity and pressure, respectively, and the bar over the variable denotes filtering. The influence of the small scales of the turbulence on the large energy-carrying scales in Eq. 2 appears in the SGS stress tensor, $\tau_{ij} = \overline{u_i u_j} - \overline{u}_i \overline{u}_j$. The algebraic eddy viscosity model originally proposed by Smagorinsky [19] is used in the present work for its simplicity and low computational cost. The Smagorinsky model represents the anisotropic part of the SGS stress tensor, τ_{ij}, as:

$$\tau_{ij} - \frac{1}{3}\delta_{ij}\tau_{kk} = -2\nu_{sgs}\overline{S}_{ij} \tag{4}$$

where $\nu_{sgs} = (C_s \Delta)^2 \left|\overline{S}\right|$ is the SGS viscosity and

$$\overline{S}_{ij} = \frac{1}{2}\left(\frac{\partial \overline{u}_i}{\partial x_j} + \frac{\partial \overline{u}_j}{\partial x_i}\right) \tag{5}$$

is the resolved rate-of-strain tensor and $\left|\overline{S}\right| = 1/2\left(2\overline{S}_{ij}\overline{S}_{ij}\right)^{\frac{1}{2}}$. The Smagorinsky constant of $C_S = 0.1$ was used in the present work. Equations 2 and 3 are discretized using a commercial finite volume solver, AVL FIRE, to solve the incompressible Navier-Stokes equations using a collocated grid arrangement. The convective fluxes are approximated by a blend of 95% central differences of second-order accuracy and 5% upwind differences. The time integration is done using the second-order accurate three-time level scheme.

Figure 2b presents the computational domain. The square cross section of the computational domain corresponds to that of the wind tunnel used in [18] and the blockage ratio is 3%. The model is placed such that the center of volume of the model corresponds to the center of the cross section. The length from the inlet to the nose of the model is 8H and from the base of the model to the outlet is 20H, which are the same relations as are used in LES of similar bluff body flows [4, 5, 7]. A uniform streamwise velocity of U_o = 7.85 m/s is used as the boundary condition at the inlet. The reason for the difference between the inlet velocity in the experiment [18] and the present simulations is that water was used in the experiment and air in the present simulation. Thus, to obtain the same Reynolds number, the inlet flow velocity was increased in the simulations. The homogeneous Neumann condition is used at the outlet. The no-slip condition is used to simulate the walls in the wind tunnel experiments at the

surrounding boundaries. Blowing and suction at the control slot are simulated by using a normal velocity for the cells occupying the slot.

The resolution requirements of the simulations were controlled by performing all simulations on two computational grids. In total, four computational grids were used in the simulations: one coarse and one fine grid for the natural case and one coarse and one fine for the controlled cases. The grids were made with the commercial grid-generator software Ansys ICEM-CFD. They contain only hexa-hedral elements. The part of the grid is shown in Fig. 3.

Block-structured computational grids were used in the simulations. In the natural case, 5×10^6 and 7×10^6 nodes were used in the coarse and the fine grids, respectively. In the controlled cases, 6×10^6 and 9×10^6 nodes were used in the coarse and fine grids, respectively.

The spatial resolution in the simulations is presented in Table 1. The resolution in both the wall-normal direction (n_+) and the directions (s_+) perpendicular to the streamwise direction (x_+) is very good for the entire model. The resolution in the streamwise direction is $x_+ < 50$ on the first 2/3 of the model's length in all the simulations and the maximum value shown in Table 1 occurs at the last third of the model. The convergence of the simulations was found to be very sensitive to the CFL number at the front of the model where the maximum CFL numbers were located. To keep the CFL number below 1, a non-dimensional time step, $\Delta t^* = U_o \Delta t/H$, of 0.004 was used in the natural simulations. In the controlled case simulations, Δt^* was 0.003. This time step resulted in maximum CFL numbers of approximately 2 in all the simulations. Furthermore, the CFL number is smaller than 1 in 99% of all the computational cells during the entire simulation. All simulations were run until the values of the aerodynamic coefficients stabilized before averaging was initiated. The averaging in the simulations was initiated after $t^* = 40$. The averaging for either the natural or the controlled flow was made during $t^* = 360$ except in the controlled case using tangential blowing of $V_b = 0.5U_o$ where the averaging was made during $t^* = 500$.

The number of computational cells in the actuation region is an important parameter for accurate prediction of the actuated flow. A previous LES study by Krajnović and Fernandes [3] of actuated flow used 5×9 computational cells in the streamwise/transverse and spanwise directions for the resolution of the flow around each slot. In the present work, 120×8 computational cells were used in the directions of the A-pillar and the orthogonal directions to the A-pillar, for the resolution of the flow around the slot.

Table 1. Spatial resolution on the body in the present LES simulations

Case	$\mathbf{n^+}$	**Mean** ($\mathbf{n^+}$)	$\mathbf{s^+}$	$\mathbf{x^+}$
Natural coarse	$n^+ < 2.3$	0.37	$s^+ < 10$	$x^+ < 100$
Natural fine	$n^+ < 2$	0.38	$s^+ < 7.5$	$x^+ < 80$
Control coarse	$n^+ < 2$	0.4	$s^+ < 10$	$x^+ < 100$
Control fine	$n^+ < 1.8$	0.4	$s^+ < 7.5$	$x^+ < 80$

The Smagorinsky subgrid-scale model is very dissipative and therefore not properly predict the evolution of the separated shear layer. However, the contribution of the subgrid-scale stresses in the region of shear layers was small in the present work. This is reflected by the ratio of subgrid-scale to laminar viscosity which was found to be $\upsilon_{sgs} / \upsilon \leq 1$ in the shear layer separating forming the longitudinal vortices as seen in Fig. 4.

The results on two computational grids were compared for the resulting velocities and aerodynamic forces. An example of the comparison of velocities along the trailing vortices is shown in Fig. 5. Differences in the velocities between different grids are small and the largest differences were found for the flow with blowing actuation. This is expected as the tangential blowing increases the CFL number and thus requirements for resolution.

Table 2 shows comparison of the aerodynamic forces between results using different computational grids. The difference in the drag coefficient between the two computational grids is less than 1.4% in all cases proving the grid convergence of the results.

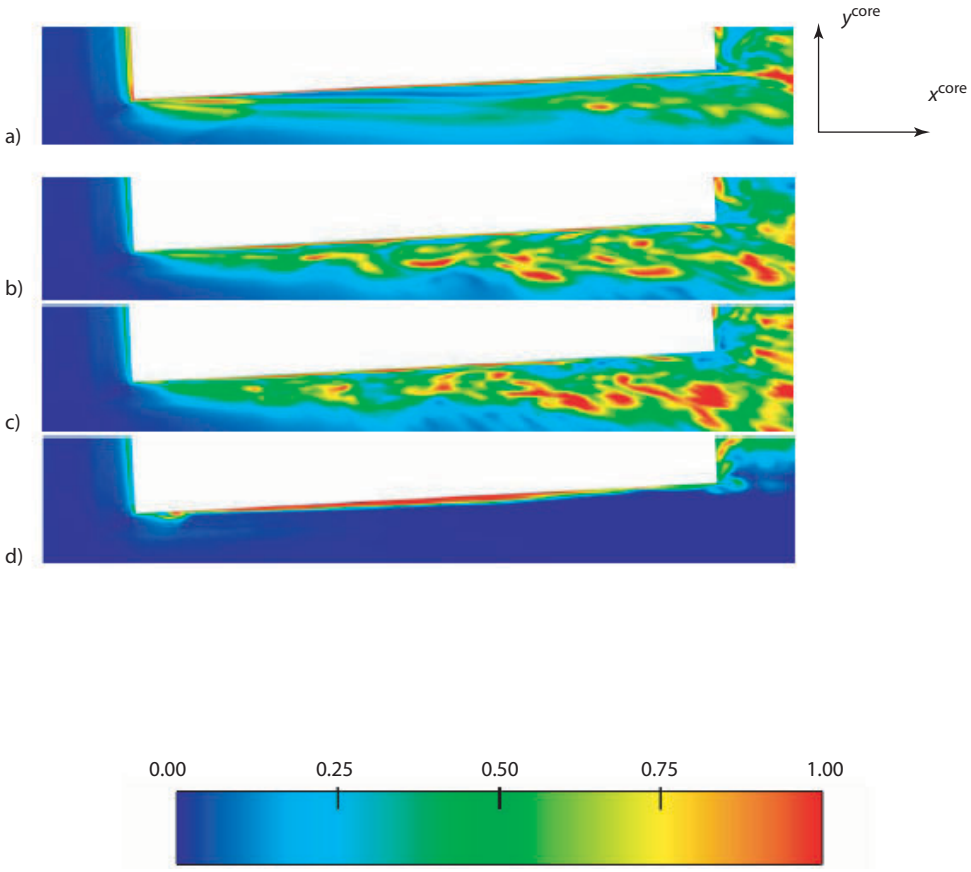

Figure 4. Plots showing the SGS viscosity (Eq (4)) divided by molecular viscosity, $\upsilon_{sgs}/\upsilon \leq 1$, for the four cases (fine grids) in the longitudinal plane through the vortex core., a) natural flow, b) actuation with blowing $V_b = 0.5\ U_0$, c) actuation with blowing $V_b = U_0$, d) actuation with suction $V_s = -U_0$. View is from above.

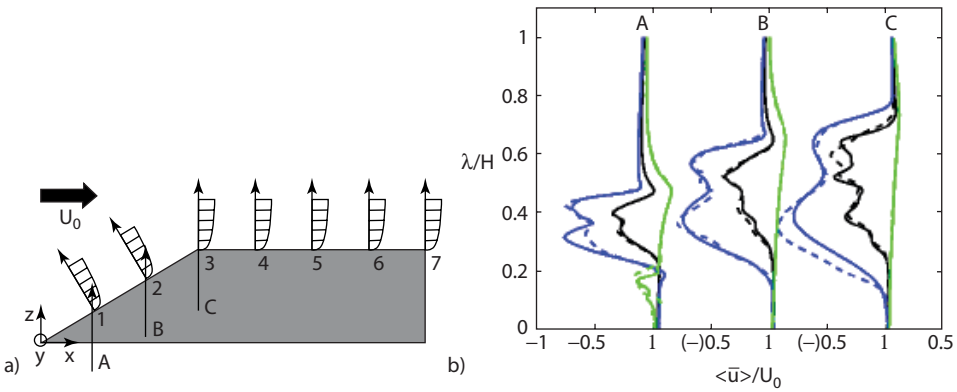

Figure 5. a) Location of the velocity profiles along the longitudinal vortex. b) Profiles of the stream wise velocity for flow (black lines), blowing $V_b = U_o$ (blue lines) and suction $V_b = -U_o$ (green lines). The dashes lines are the coarse meshes and the drawn lines are the fine meshes, respectively. The lines A, B and C are placed vertically through the vortex on the side of the model.

Table 2. Drag force on the body from the simulations compared with experimental results from [18]. ΔC_D^1 are the differences between the computed and the experimental values. ΔC_D^2 are the differences between the coarse and fine grids and ΔC_D^3 are the differences between the control cases and the natural case

Aerodynamic coefficients	C_D	RMS(C_D)	ΔC_D^1	ΔC_D^2	ΔC_D^3
Natural exp	0.55	0.08	–	–	–
Natural fine	0.487	0.005	–11.5%	–	–
Natural coarse	0.480	0.005	–12.7%	–1.4%	–
Control $V_S = -U_0$ exp	0.52	–	–	–	-5.5%
Control $V_S = -U_0$ fine	0.433	0.004	–16.7%	–	-11.1%
Control $V_S = -U_0$ coarse	0.429	0.007	–17.5%	–0.9%	-10.6%
Control $V_B = U_0$ exp	0.594	–	–	–	+8%
Control $V_B = U_0$ fine	0.497	0.006	–16.3%	–	+2%
Control $V_B = U_0$ coarse	0.503	0.008	–15.3%	+1.2%	+4.8%
Control $V_B = 0.5\ U_0$ exp.	≈0.55	–	–	–	≈0%
Control $V_B = 0.5\ U_0$ fine	0.496	0.005	–9.8%	–	+2%

6. RESULTS

6.1 Comparison of the experimental and LES velocity fields and global quantities

Figures 6 and 7 show the comparison of the stereo-PIV results from Lehugeur et al. [18] with the present LES results. The velocity vectors in planes x/L=0.12, 0.24, 0.35, 0.41, 0.47 and 0.59 are shown together with the cartographies of non-dimensional mean velocity U_x (the velocity along the x axis) over the free-stream velocity U_o for the natural flow and the flow actuated with tangential blowing using $V_b = 0.5U_o$. The position of the vortex along the x axis in both the natural and the actuated flow from the present LES was found to be in very good agreement with the experimental one. However, differences were observed in the level of non-dimensional mean velocity U_x/U_o. As the experimental and LES pictures were made using different color scales, it is not clear whether the differences in U_x/U_o are real differences in the results or a consequence of different coloring.

The mean and the root mean square (RMS) of the drag force coefficient are presented in Table 2. In all cases there is a difference of some 10-17% between the experimental and numerical values of the drag. The origin of this difference is not clear and may be due to the difference between the experimental and the numerical set-ups as the egg-shaped section support of the model used in the experiment was omitted in the present simulation. This support of course contributes drag to the total drag due its influence on the flow below the body, which manifests for example in horseshoe vortices around the support on the bottom surface of the vehicle model. The last column in Table 2 shows the difference between the drag coefficients of the natural and controlled flows. The trends in the change of the drag coefficient as a result of the actuation in all simulations are the same as in the experiments. The differences in the percentage of the drag change are again attributed to the differences between the experimental and numerical set-ups, as the contribution of the support to the drag represents a different percentage of the drag coefficient in different cases.

Besides the differences in the experimental and numerical set-ups, there are other numerical sources of errors. These are caused by the upwinding (although only a small contribution of 5%) used in the spatial discretization. The numerical damping caused by upwinding may be one possible reason why the RMS values of the drag coefficient in the natural flow are one magnitude lower in the LES compared with the experimental value.

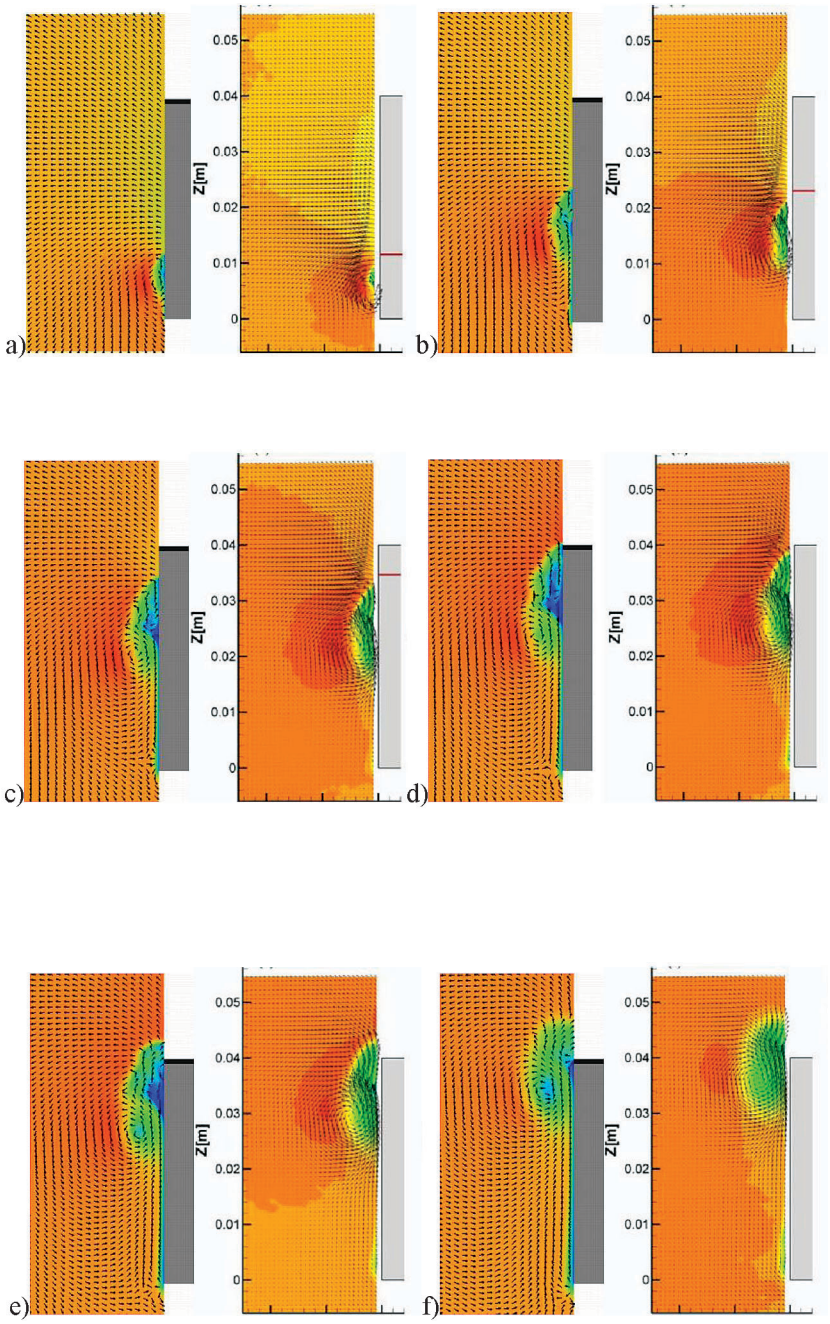

Figure 6. Comparison of the mean velocity vectors and the U component for the case without control, left longitudinal vortex, back view. a) x/L=0.12, b) x/L=0.24, c) x/L=0.35, d) x/L=0.41, e) x/L=0.47, f) x/L=0.59. LES (left figure) and PIV (right figure).

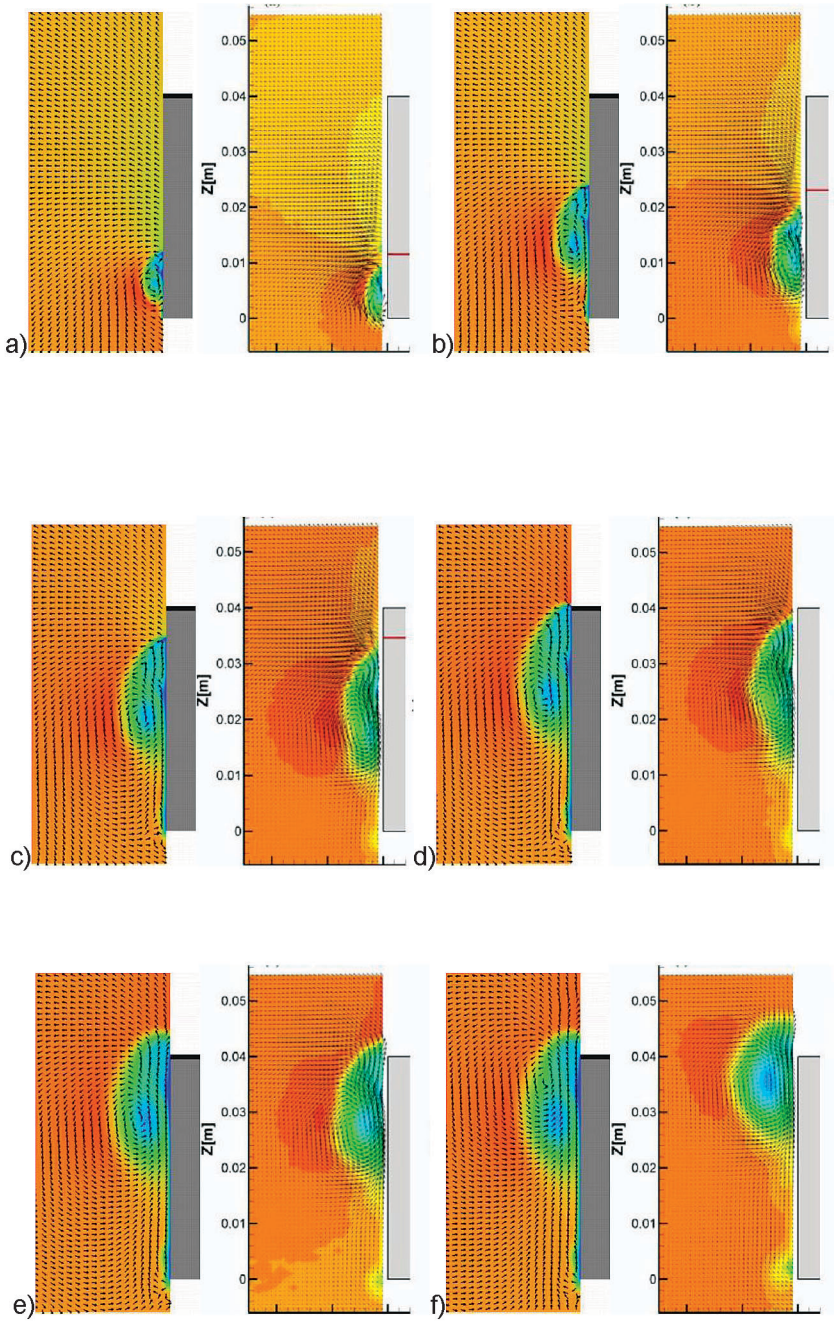

Figure 7. Comparison of the mean velocity vectors and the U component for the case with blowing $V_b = U_o$, left longitudinal vortex, back view. a) x/L=0.12, b) x/L=0.24, c) x/L=0.35, d) x/L=0.41, e) x/L=0.47, f) x/L=0.59. LES (left figure) and PIV (right figure).

6.2 Influence of actuation on the longitudinal vortices

Here we discuss the influence of the actuation on the flow around inclined edges and its influence on the formation of longitudinal vortices.

Figure 8a shows how the shear layer rolls into the longitudinal vortex in the case without flow actuation. This figure reveals that the trailing vortex consists of two different parts, one with a columnar shape stretching from the leading edge of the body approximately to the position of the leading edge of the roof, and one in which the vortex is broken down (after the approximate position of the leading edge of the roof). The difference between the two flow regimes is typical for a vortex breakdown-process where the columnar part of the vortex is characterized by a strong longitudinal and swirl velocity component that rapidly decreases at the position of breakdown, resulting in a sudden expansion of the vortex diameter and its breakdown. Adding the momentum to the shear layer in Figs. 8b and 8c where tangential blowing is applied results in an earlier change of the vortex state. This is in agreement with the actuation hypothesis used in the present work that suggested that adding the vorticity in the shear layer will increase the swirl of the vortex and promote earlier breakdown of the longitudinal vortex. The tangential suction with $V_b = -U_o$ used in Fig. 8d reduced the vorticity in the shear layer and weakened the vortex to such an extent that it exists only in the very short distance from the leading edge to the position of the actuation slot (see Fig. 2). The observations of the influence of tangential blowing and suction are in agreement with previous observations made by Lehugeur et al. [18] who achieved visualization by dye emissions.

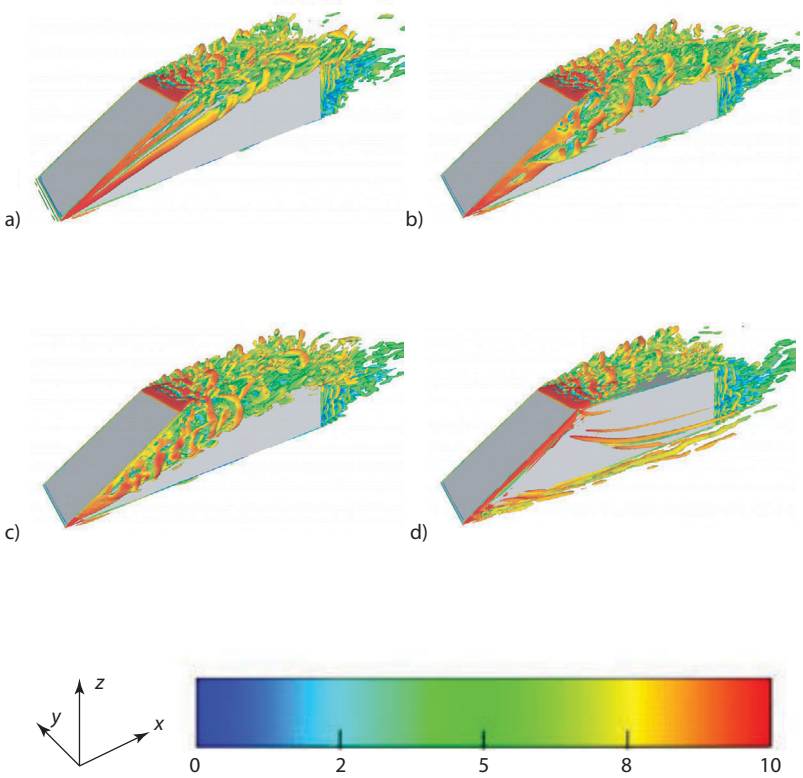

Figure 8. Second invariant of the velocity gradient $Q = 3 \times 10^5$ on the side of the model with the actuation slot. a) natural flow, b) actuation with blowing $V_b = 0.5U_o$, c) actuation with blowing $V_b = U_0$ and d) actuation with suction $V_b = -U_o$. The legend is of the velocity magnitude in m/s.

The influence of the actuation on the flow evolution along the slanted surface and the roof is presented in Fig. 9. The actuation using suction has noticeable influence on the flow field along the slanted surface at the positions parallel with the actuation slot (positions 1 and 2). The influence of the actuation is smaller at positions 3-4 due to the presence of the separation bubble in this region that dominates the flow. At the downstream positions 5-6, the flow is dominated by the broken trailing vortices with different velocity fields for natural and actuated flows. Also here the largest difference between the actuated and the natural flow is for the case of suction which eliminates one of the trailing

vortices. The spanwise velocity component $\langle \bar{v} \rangle$ in Fig. 9c for the case of suction is very different from other three cases due to large asymmetry in the flow caused by the elimination of one of the trailing vortices.

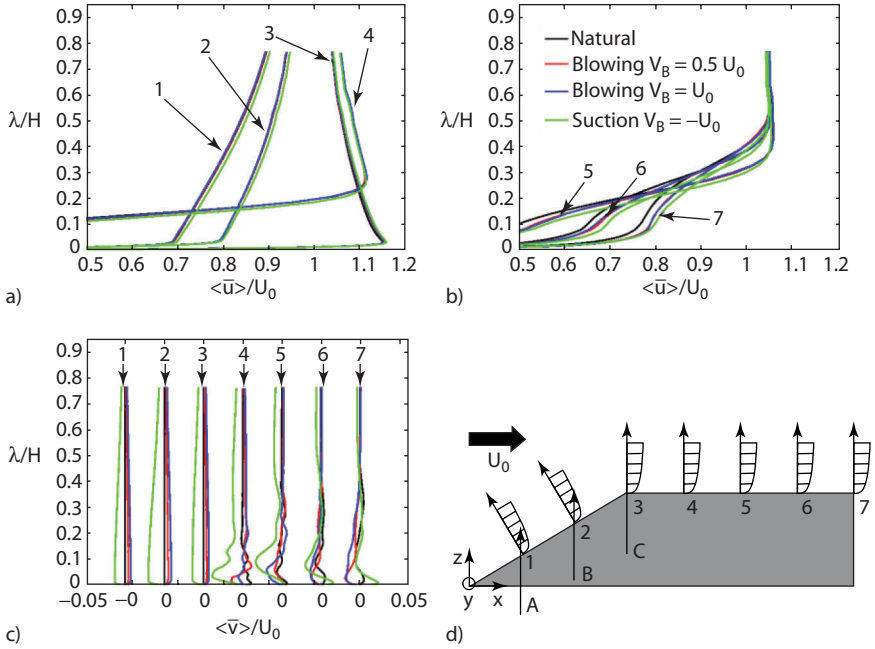

Figure 9. Profiles for the streamwise ($\langle \bar{u} \rangle$) and the spanwise ($\langle \bar{v} \rangle$) mean velocity components at seven lines along the y symmetry plane of the body. The velocities are plotted versus the length of the lines, λ, divided by the height of the body, H. a) $\langle \bar{u} \rangle$ plotted versus the length of the lines 1 – 4. b) $\langle \bar{u} \rangle$ plotted versus the length of lines 5 – 7. c) $\langle \bar{v} \rangle$ plotted versus the length of lines 1 – 7. d) The placement of the lines along the y symmetry plane. $\langle\ \rangle$ denotes time-averaging.

An interesting observation in the present work is that the actuation on the left side of the model influences not only the flow near the actuation slot but also the longitudinal vortex on the right side of the model where no actuation was applied. Note that the influence of the actuation on the right side of the model is much smaller from that on the left (actuated) side of the model. Figure 10 shows the second invariant of the velocity gradient colored with vorticity in the direction of the time-averaged vortex core shown in the figure. Figures 10d, 10e and 10g show that the vortex breakdown on the side of the body without an actuation slot occurs earlier when blowing or suction is applied on the opposite side. In particular the case with blowing $V_b = U_o$ shows premature vortex breakdown on the uncontrolled side (Fig. 10f). This is of course not very strange considering the elliptic character of the solved equation. However, this is worth keeping in mind in practical applications of the present actuation strategy, where an appropriate level of actuation must be chosen (to avoid unexpected lateral forces that could cause directional instability).

Another observation from Fig. 10 is the existence of secondary vortices with a direction of rotation opposite to that of the main longitudinal vortices. Such secondary vortices were not reported in Lehugeur et al. [18] as the resolution of their PIV measurements near the wall of the model was not fine enough (Lehugeur et al. [18]). However, secondary vortices similar to those found in the present work were found in a numerical simulation by Lehugeur et al. [20] although the angle of the slanted surface was 40° compared to the 30° in the present paper. Further, the PIV by Levy et al. [11] using finer PIV resolution was successful in resolving the secondary longitudinal vortices around the A-pillar inclined at the same angle of 30° as in the present paper. Similar secondary vortices were also detected in PIV by de Moraes et al. [10]. We shall return to these secondary vortices in the discussion of the results of the time-averaged flow.

Figure 10a-b shows the existence of at least three regions of strong Q values. The first is located in the center of the primary longitudinal vortex. The second is located in the center of the secondary vortex and has a direction of the rotation opposite to that of the primary vortex. The origin of this

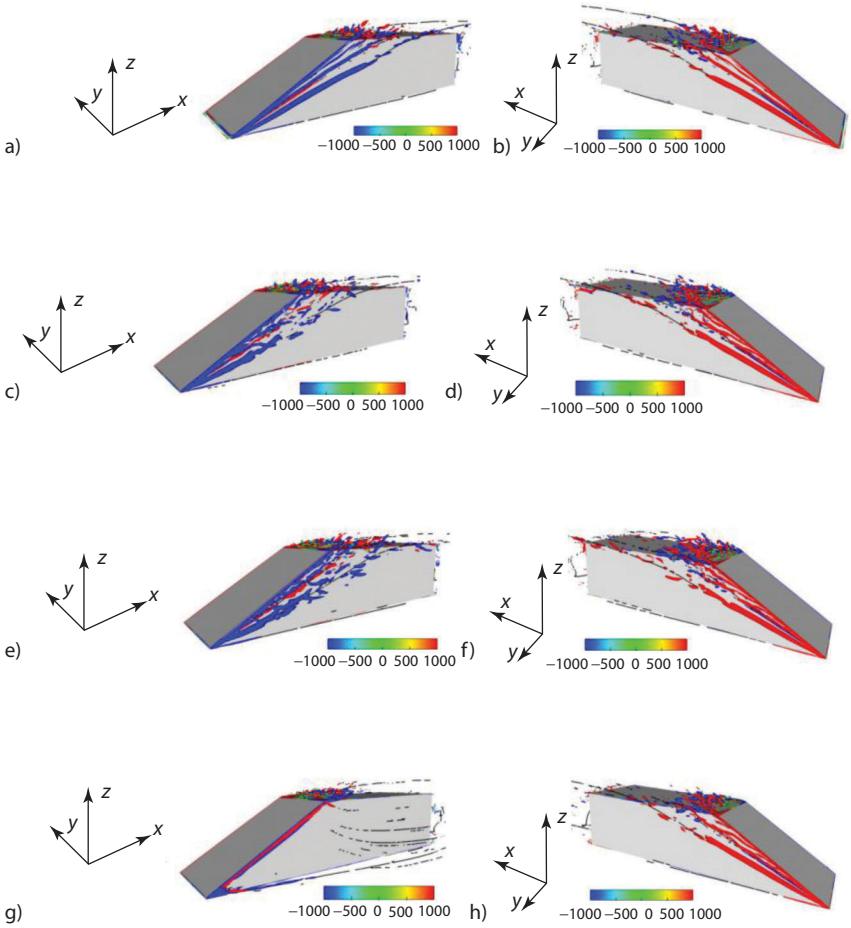

Figure 10. Second invariant of the velocity gradient Q = 4 × 10^6 on the side of the model with and without actuation slot. a–b) natural flow, c–d) actuation with blowing $V_b = 0.5U_o$, e–f) actuation with blowing $V_b = U_o$ and g–h) actuation with suction $V_b = -U_o$. The legend is of the velocity component in the direction of the vortex core, x^{core}.

secondary vortex is boundary layer separation on the lateral side of the body due to the adverse pressure gradient caused by the primary vortex. As the separated boundary layer hits the separated shear layer from the A pillar, the third region of strong Q is formed, colored with the same vorticity orientation as that in the core of the primary longitudinal vortex. The instantaneous secondary vortex dissipates faster than the primary one (see Fig. 10a-b).

The instantaneous flow field structure on a plane passing through the vortex axis is displayed in Fig. 11 in terms of vorticity magnitude. The shear layer, which is initially straight, is observed to attain a wavy form after some distance. At approximately the same position of this transformation of the shear layer, the core of the vortex containing high level of vorticity breaks down into discrete regions of high vorticity.

Figure 12 shows the instantaneous vorticity magnitude in a plane passing through the vortex axis but orthonormal to the plane from Fig. 11. The longitudinal vortex contains two linear regions (upper and lower) of high vorticity in the natural flow in Fig. 12a. Although the upper high vorticity region seems to show instability in the natural flow, the actuation of the surrounding shear layer of the vortex when blowing is applied in Fig. 12b-c influences the entire vortex, resulting in a growth of the vortex core and a decrease in vorticity.

Contours of instantaneous axial vorticity at several cross flow planes along the longitudinal vortices are shown in Fig. 13. The natural flow produces an instantaneous primary longitudinal vortex that preserves its columnar shape along the entire length of the A-pillar and only first at a location behind it (x/d=1.2) shows signs of a changed structure. It grows in diameter along the A-pillar as its axial vorticity decreases. Tangential blowing already influences the vortex at x/d=0.4 and while the blowing with $V_b = 0.5U_o$ changes the shape of the structure only a little, blowing with $V_b = U_0$ results in a large change in the vorticity distribution, and the spontaneous vortex breakdown is initiated

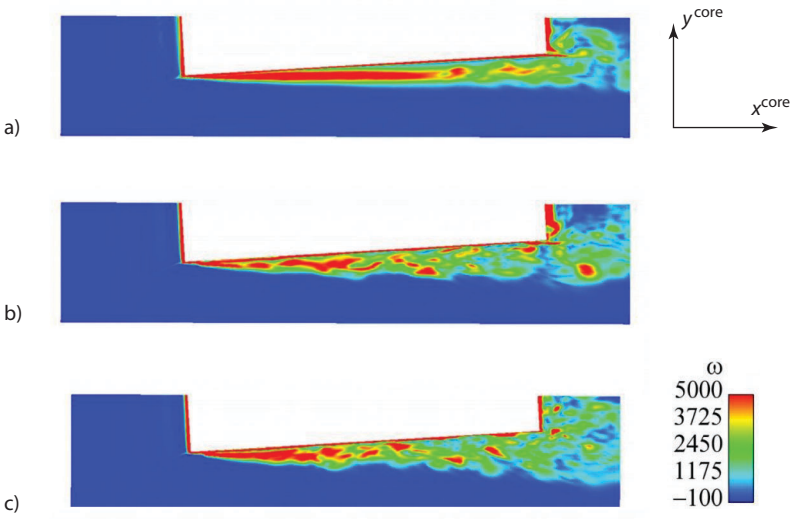

Figure 11. Instantaneous vorticity magnitude in the longitudinal plane through the vortex core. a) natural flow, b) actuation with blowing $V_b = 0.5U_o$, c) actuation with blowing $V_b = U_o$. View is from above.

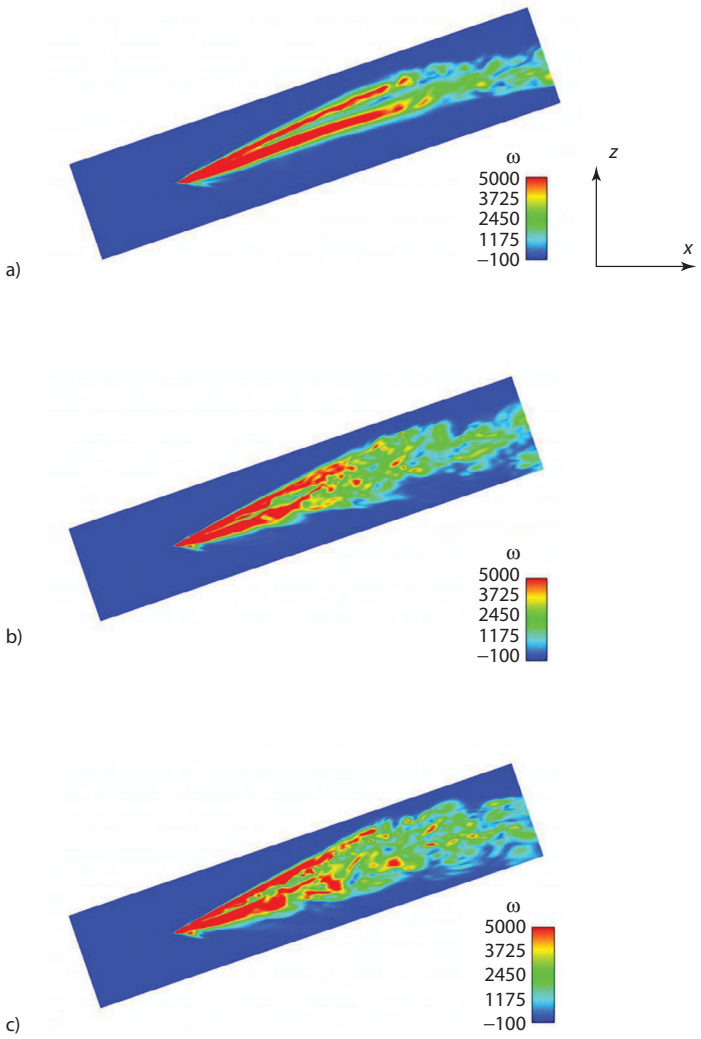

Figure 12. Instantaneous vorticity magnitude in the longitudinal plane through the vortex core. a) natural flow, b) actuation with blowing $V_b = 0.5U_o$, c) actuation with blowing $V_b = U_o$. Side view.

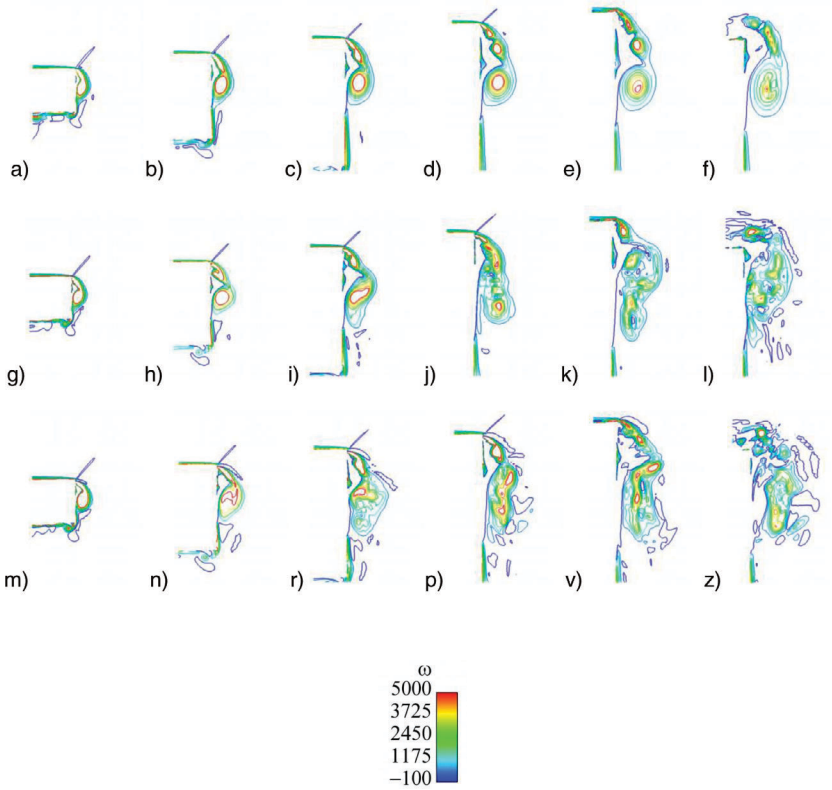

Figure 13. Magnitude of instantaneous vorticity in planes orthonormal to the vortex core. a–f) natural flow, g–l) actuation with blowing $V_b = 0.5U_o$, m–z) actuation with blowing $V_b = U_o$. View is from above. Cross flow planes are, from left to right, x/D=0.2, 0.4, 0.6, 0.8, 1.0 and 1.2.

6.3 Time-averaged flow

Figure 14 shows a side view of the body with trace lines on the body surface and the vortex cores of the time-averaged flow in four different cases. Early on, Watanabe et al. [21] described two types of vortex flows on the lateral side of the A-pillar from an oil film visualization. According to them, the main flow separating behind the A-pillar reattaches at the side window making the reattachment line. The second bifurcation line, the stagnation line, was found in Watanabe et al. [21] further left of the reattachment line, showing the border between the main and the secondary longitudinal vortices. These separation and reattachment lines are shown in Fig. 14a. Both lines in the figure are found to be straight lines with trace lines in between that culminate in a stable focus structure. The flow on the surface of the body in Fig. 14 changes when tangential blowing is applied (Fig. 14b-c). The trace lines in the case of blowing with $V_b = 0.5U_o$ show a wavy structure in the region of the reattachment of the primary longitudinal vortex on the surface of the body. Furthermore, a sudden change of the vortex was observed at the approximate position of the leading edge of the roof of the body displayed in Fig. 14b, caused by a sudden change of the height of the vortex core (but with the same slope of the core). This flow behavior is in agreement with the more unstable flow in the case with $V_b = 0.5U_o$ and, although averaging was continued for almost twice the time used for the other cases, the shape of the flow structures was preserved. On the other hand, suction resulted in an elimination of the longitudinal vortices and a very different flow from that found in the other cases (Fig. 14d). The coloring of the body surface with the pressure coefficient in Fig. 14 shows a slightly higher pressure in the case of $V_b = 0.5U_o$ compared with $V_b = U_o$ and a natural flow that has an influence on the overall drag.

Figure 15 shows the trace lines on the upper side. The case with suction shows different flow on the roof of the body where the flow separates in all cases but the separation bubble is wider in the case with suction. This is also confirmed with lower pressure in Fig. 15d.

The vortex core was in agreement with previous observations in which it was found not to be aligned with the edge of the A-pillar [11,20]. The vortex core of the primary longitudinal vortex was found to be positioned at angles of α =19.1° and β = 3.6°. It is interesting that these two angles did not change

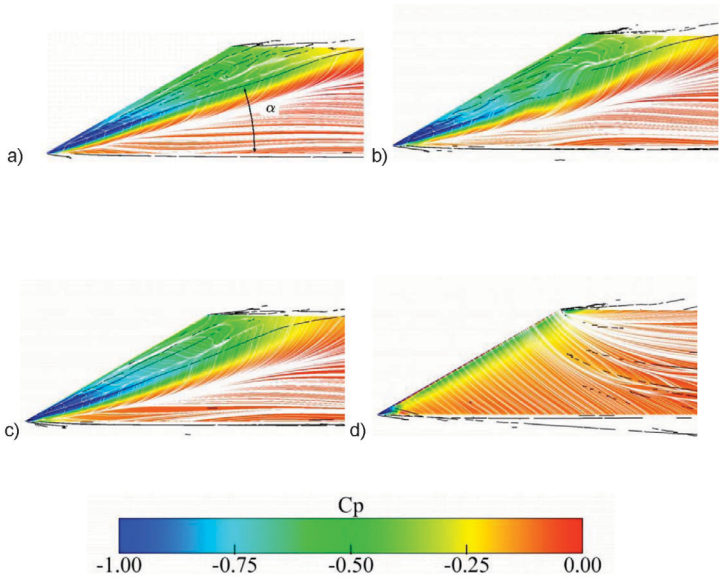

Figure 14. Time-averaged flows for natural (a) and controlled flows using $V_b = 0.5U_o$ (b), $V_b = U_o$ (c) and $V_b = -U_o$ (d). Figure show a view from the left side of the body and vortex cores and particle traces on the body surface. The body is colored with the surface pressure coefficient.

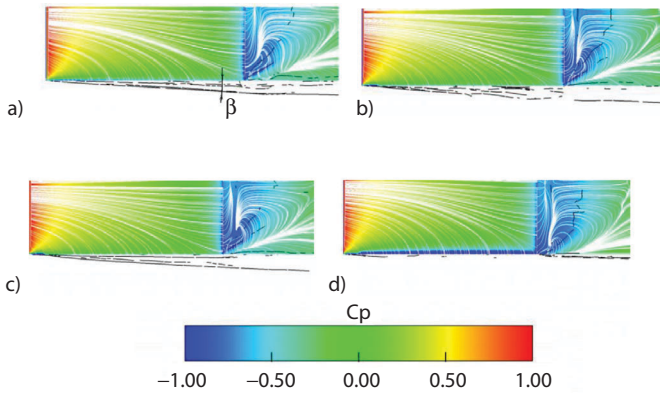

Figure 15. Time-averaged flows for natural (a) and controlled flows using $V_b = 0.5U_o$ (b), $V_b = U_o$ (c) and $V_b = -U_o$ (d). Figure show a view from above the body and vortex cores and particle traces on the body surface. The body is colored with the surface pressure coefficient.

very much in the cases with natural flow and blowing. Although the angle of the secondary vortex is smaller than that of the primary one ($\beta = 1.5°$ compared with $\beta = 3.6°$), it is not zero, as suggested by Levy et al. [11] (see Fig. 15).

Figures 16 and 17 show comparison of the time-averaged longitudinal vortices formed along the A-pillar with the actuation slot in the case of natural flow and blowing with $V_b = U_o$, respectively. Figure 16 shows the difference in the levels of the vorticity component along the vortex core of the main longitudinal vortex. Adding momentum by tangential blowing into the shear layer (Fig. 16b) increases the overall vorticity in the longitudinal vortex. Besides the difference in the size of the coherent structures on the side of the A-pillar between the natural flow and the actuated flow, the topology also seems to differ. While three different longitudinal vorticies are visible in the case of the natural flow, the third vortex located above the main longitudinal vortex is more difficult to see when blowing is applied.

The axial velocity component is much higher in the natural flow than in the flow with tangential blowing (Fig. 17). The reason is found in the earlier vortex breakdown in the actuated flow, as can be seen in the distribution of the axial velocity component in Fig. 18. While the plateau in the normalized axial velocity U_x^{core}/U_o along the vortex core occurs at x/D=1.2 in the natural flow, the same happens much earlier (approximately at the position of the start of the slot) in the flow with blowing. Figure 18

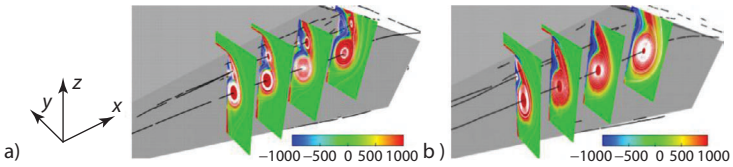

Figure 16. Time-averaged axial vorticity in planes x/L=0.2682, 0.3236, 0.3956, 0.5011. a) natural flow, b) actuation with blowing $V_b = U_o$.

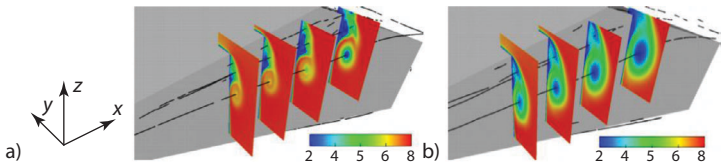

Figure 17. Time-averaged axial velocity in planes x/L=0.2682, 0.3236, 0.3956, 0.5011. a) natural flow, b) actuation with blowing $V_b = U_o$.

also shows that the axial velocity has a sinusoidal behavior along the vortex core in the case using blowing of $V_b = 0.5U_o$ showing more of an irregular shape of the longitudinal vortex in that case. The corresponding distribution to that of the axial velocity along the vortex on the actuated side of the model is presented in Fig. 18 on the side of the body without actuation. While the natural flow shows very similar flow structures on both sides (shown in Fig. 18 in blue), the longitudinal vortex on the side with no actuation in both cases with blowing becomes unstable at approximately x/D = 0.7, in agreement with previous observations of differences in the instantaneous flow on this side of the body.

Figure 19 shows the time-averaged flow around the A-pillar without the actuation slot. One can also see here that the flow structures are disturbed by the blowing on the opposite side of the body and that the axial velocity decreases, indicating the premature vortex breakdown.

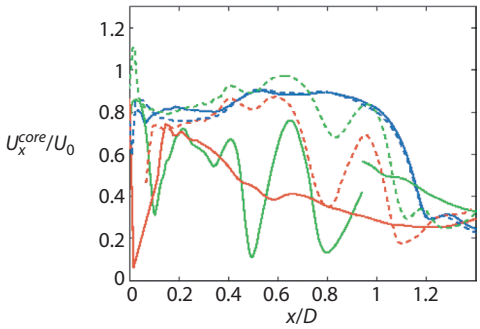

Figure 18. Distribution of the normalized axial velocity along the A-pillar. Natural flow (blue); blowing using $V_b = 0.5U_o$ (green) and blowing using $V_b = U_o$ (red). The solid line and dashed lines are on the side with actuation and without actuation, respectively.

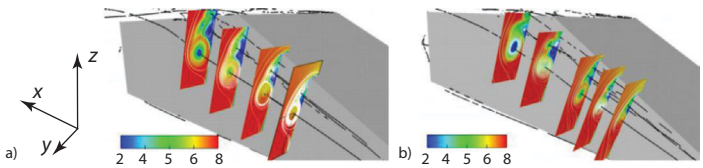

Figure 19. The flow around the side without actuation slot. Time-averaged axial velocity for a) natural flow in planes x/L=0.2682, 0.3236, 0.3956, 0.5011. b) actuation with blowing $V_b = U_o$ in planes x/L=0.2292, 0.2682, 0.3236, 0.3956, 0.5011.

6.4 Time-averaged vorticity and swirl number

Time-averaged axial vorticity in Fig. 20 shows that the natural flow averages to longitudinal vorticies that are similar to those found in the instantaneous flow in Fig. 13. Again we observe a decrease in the magnitude of the axial vorticity associated with the deceleration of the vortex swirl and its breakdown. This is even more visible for the actuated flow, where for example the structure of the vortex is highly distorted at x/D=0.8 for actuation using $V_b = 0.5U_o$. Tangential blowing using $V_b = U_o$ already has a large impact at position x/D=0.4 with a large decrease in axial vorticity. Note that the secondary vortex remains qualitatively similar in all planes. Furthermore, actuation seems to have little influence on that vortex. This region seems not to be influenced by vortex breakdown or tangential blowing.

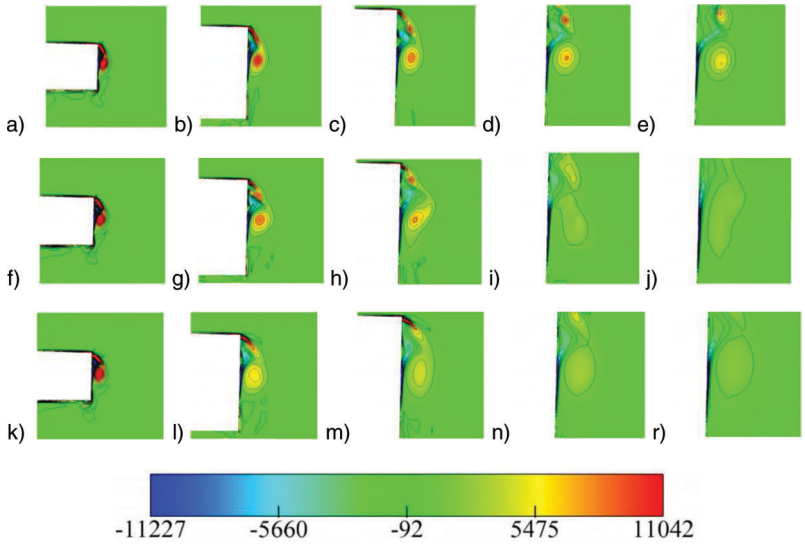

Figure 20. Time-averaged axial vorticity in planes orthonormal to the vortex core. a–e) natural flow, f–j) actuation with blowing $V_b = 0.5U_o$, k–r) actuation with blowing $V_b = U_o$. View is from above. Cross flow planes are, from left to right, x/d=0.2, 0.4, 0.6, 0.8 and 1.0.

An important parameter in the study of vortex breakdown is the ratio of the azimuthal and axial velocity $S = U_\theta / U_x^{core}$. The maximum value of this ratio, often called the swirl number, is used in vortex breakdown experiments on swirling jets to find when the vortex breakdown will occur. For example in [22] it was found that when the swirl number exceeds the critical value of 1.5 the swirling jet confined in the cylindrical duct undergoes vortex breakdown.

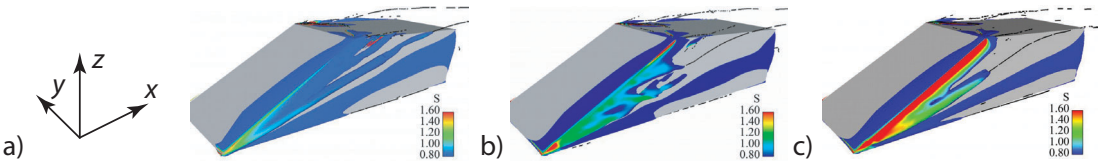

Figure 21. An isosurface of the axial vorticity $\omega_x^{core} = 2.6 \times 10^3$ colored with the ratio of the azimuthal and axial velocity $S = U_\theta / U_x^{core}$. a) natural flow, b) actuation with blowing $V_b = 0.5U_o$, c) actuation with blowing $V_b = U_o$.

It is not clear in the present case where along the longitudinal vortex the swirl number should be computed as there is no natural position such as that of the orifice from which the swirling jet is generated in [22]. However, the ratio of $S = U_\theta / U_x^{core}$ as is shown in Figs. 21 and 22 shows the differences in the breakdown position between the natural flow and the flow with blowing. This ratio is increased in the shear layer of the vortex and goes up to some 1.2 in the case with $V_b = 0.5U_o$ (Fig. 21b). The value in the case with $V_b = U_o$ is 1.6, showing that the swirl motion dominates the entire vortex. Figure 22 shows that the natural flow exhibits a high value of S=1.5 first very late in the development of the longitudinal vortices (x/D=1.0) and then, in contrast to in the shear layer of the primary vortex in the actuated flow, in the shear layer of the secondary vortex. On the other hand, the same level of S was already obtained at the beginning of the vortex (x/D=0.2) when blowing was applied.

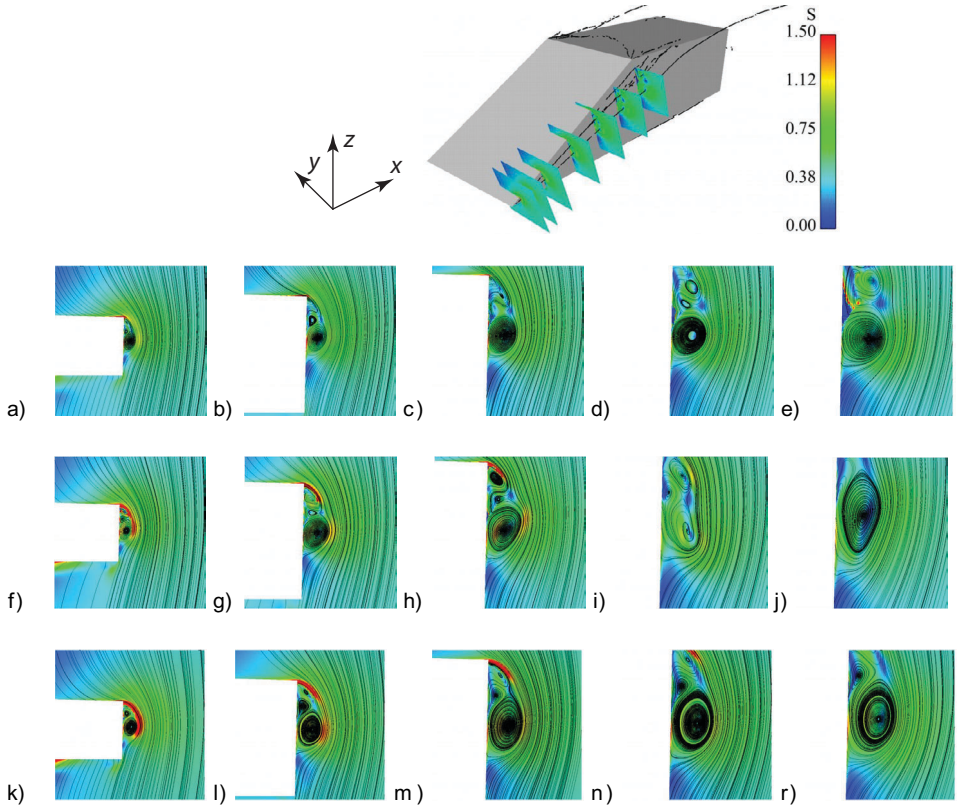

Figure 22. Ratio of the azimuthal and axial velocity $S = U_\theta / U_x^{core}$. a-e) natural flow, f-j) actuation with blowing $V_b = 0.5U_o$, k-r) actuation with blowing $V_b = U_o$. Cross flow planes are, from left to right, x/D=0.2, 0.4, 0.6, 0.8 and 1.0. The upper figure shows the position of the planes.

6.5 Temporal properties of the aerodynamic forces and the fluctuating velocity and pressure

In the case of natural flow, Lehugeur et al. [18] analyzed the signal of the drag using Power Spectral Density (PSD). Their PSD showed a peak corresponding to a Strouhal number $St = Wf/U_o$ of 0.2. The PSD of the natural flow drag signal shows several peaks of which the highest frequency corresponds to St =0.1. However the lift force signal PSD shows a very strong peak at approximately St =0.23. This is in agreement with previous LES by Krajnovic and Davidson of flows around a bus [2] model and the Ahmed body [4-5]. For example in LES of the bus flow [2], the side force signal had a dominant frequency corresponding to St =0.22. The lift force signal in the Ahmed body LES [4] was dominated by the non-dimensional frequency of St =0.23. Although it is not clear why the present LES displays the high frequency motion of the wake in the lift force signal and not the drag force signal found in the experiment by Lehugeur et al. [18], a similar frequency seems to appear in several generic body flows as found in previous LES simulations [2,4-5]. The LES of the actuated flow showed that while the tangential suction decreases the energy of the dominant peak at St =0.23, the tangential blowing removed it completely, transforming the spectra to a broadband spectrum with no dominant frequencies.

The velocity and pressure signals were sampled at several points around the body. Of particular interest are points located in and around the longitudinal vortices and in the separated shear layers behind the body. Due to space limitations we show here only spectra for the streamwise velocity component at three points in and around the primary longitudinal vortex in Fig. 23. However, the spectra for the other two velocity components and pressure exhibit similar behavior. As seen in Fig. 23, the velocity fluctuation (and pressure fluctuation, which is not shown here) in the first half of the primary vortex (P2) shows a broadband spectrum with no dominant frequencies. This is in agreement with previous observations by Levy et al. [11]. However, the points in the shear layer and at the later position in the

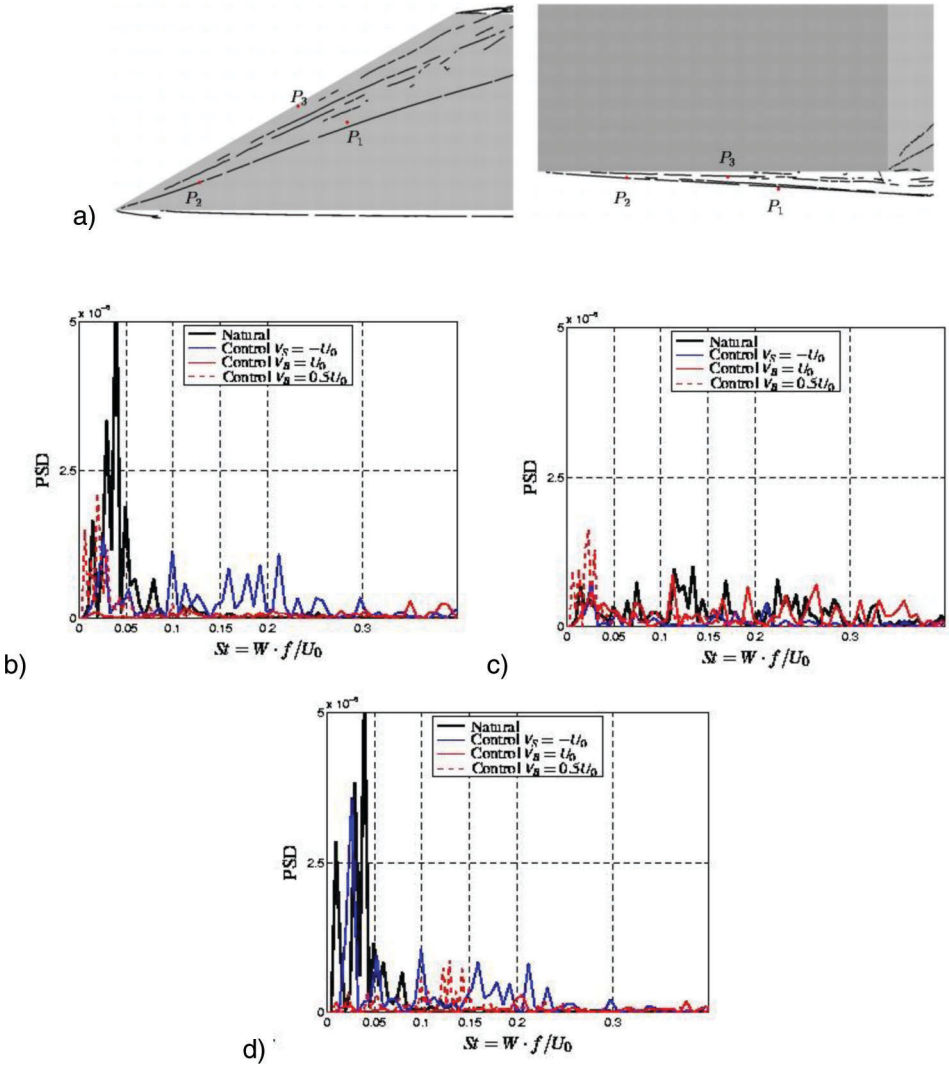

Figure 23. a) Location of the velocity samplings in and around the longitudinal vortex. Power Spectra Density of the streamwise velocity in points b) P1, c) P2 and d) P3.

primary vortex exhibit a dominant frequency of approximately St=0.04 in the natural flow. Suction in the shear layer results in a decrease of the dominant frequency to approximately St=0.025. Blowing on the other hand stabilizes the shear layer and produces a broadband spectrum (see Fig. 23d). The influence of the blowing and suction on the behavior of the primary longitudinal vortex further downstream is very different from that on the first part of the vortex. Figure 23b shows that, while blowing with $V_b = U_o$ and suction result in broadband spectrum with no dominant frequencies, the actuation using $V_b = 0.5U_o$ gives a dominant frequency at approximately St=0.02. This very low frequency of the motion of the primary longitudinal vortices results in the requirement of a very long averaging time in the present LES when tangential blowing with half of the free stream velocity was used.

7. CONCLUSIONS

The LES simulations by Krajnovic and Fernandes [3] demonstrated that LES is a useful numerical technique for exploration of the flow control mechanism when the flow control objective is to delay instability of the shear layers responsible for the formation of the wake behind the body. Although the present paper deals with control of the shear layers, the shear layer and the resulting flow structures are three-dimensional and their modification using tangential blowing requires a different strategy from that used in [3]. Perhaps the most important feature of the flow around the simplified A-pillar studied here is the vortex breakdown, which causes an increase in the cross-section of the drag inducing longitudinal vortices originating at the A-pillar and thus increases the drag of the body. The results of

the present LES show that the breakdown of this vortex is sensitive and, although it can be controlled by tangential actuation, the level of actuation is important and in some cases can result in unusual instabilities of the longitudinal vortices (such as when blowing using $V_b = 0.5U_o$). A better understanding of the modification of the flow around the A-pillar in the flow control process is of great importance, and LES is found to be a technique that is useful for this purpose.

Similar to what is shown in [3] the present work demonstrates that flow control can even have an influence in the part of the flow where it is not applied. This means that future flow control strategies must have the target of a global flow in order to be efficient.

ACKNOWLEDGEMENTS

The work presented in this paper was funded by the Chalmers Sustainable Transport Initiative. Thanks go also to AVL List GmbH for providing the licenses for the Fire AVL solver for the project. Computer time at SNIC (the Swedish National Infrastructure for Computing) at the Center for Scientific Computing at Chalmers (C3SE) is gratefully acknowledged.

REFERENCES

[1] Hucho W-H., Aerodynamic of Road Vehicles, Society of Automotive Engineers, Inc., Ed. 4, ISBN 0-7680-0029-7, 1998.

[2] Krajnović, S. and Davidson, L., Numerical Study of the Flow Around the Bus-Shaped Body, ASME: Journal of Fluids Engineering, Vol. 125, pp: 500-509, 2003.

[3] Krajnović, S. and Fernandes J., Numerical Simulation of the Flow Around a Simplified Vehicle Model with Active Flow Control, International Journal of Heat and Fluid Flow, doi:10.1016/j.ijheatfluidflow.2010.06.007

[4] Krajnović, S. and Davidson L., Flow around a simplified car, Part 1: Large eddy simulation, ASME: Journal of Fluids Engineering, Vol. 127, pp:907-918, 2005.

[5] Krajnović, S. and Davidson L., Flow around a simplified car, Part 2: Understanding the Flow, ASME: Journal of Fluids Engineering, Vol. 127, pp:919-928, 2005.

[6] Krajnović, S. and Basara B., LES of the Flow around Ahmed Body with Active Flow Control, Turbulence and Interactions Notes on Numerical Fluid Mechanics and Multidisciplinary Design, 2010, Volume 110/2010, 247254, DOI: 10.1007/978-3-642-14139-3 30.

[7] Krajnović, S. Östh J. and Basara B., LES of active flow control around an Ahmed body with active flow control, Conference on Modelling Fluid Flow (CMFF'09), The 14th International Conference on Fluid Flow Technologies, Budapest, Hungary, 9-12 September, 2009

[8] Alam F. and Watkins S. and Zimmer G., Mean and time-varying flow measurements on the surface of a family of idealized road vehicles, Experimental Thermal and Fluid Science 27, 639-654, 2003.

[9] Hoarau C., Boree J, Laumonier J. and Gervais Y., Unsteady wall pressure field of a model A-pillar conical vortex, International Journal of Heat and Fluid Flow, 29, pp:812-819, 2008.

[10] de Moraes L. F. G., Sicot C. Paille F. And Boree J., Unsteady wall pressure and velocity fields of a model A-pillar vortex. Effects of free-stream turbulence., FEDSM2010-ICNMM2010-30296.

[11] Levy B., Brancher P and Giovannini, Experimental characterization of the flow topology around a vehicle A-pillar using PIV and fluctuating wall pressure, In: 7th International Symposium on Engineering Turbulence Modelling and Measurements - ETMM7, 4-6 June 2008, Limassol, Cyprus.

[12] Onorato M., Costelli A. F. and Garrone A., Drag Measurement Through Wake Analysis, International Congress & Exposition, Detroit, Michigan, SAE Paper No. 840302, 1984.

[13] Krajnović, S., Computer Simulation of a Train Exiting a Tunnel Through a Varying Crosswind. International Journal of Railway, 1 (3 (2008.9)) pp. 99-105.

[14] Hemida H. and Krajnović, S., Exploring Flow Structures Around a Simplified ICE2 Train Subjected to a 30 Degree Side Wind Using LES. Journal of Engineering Applications of Computational Fluid Dynamics, 3 (1) pp. 28-41.

[15] Werle H., Quelques resultates experimentaux sur les ailes en fleche, aux faibles vitesses, obtenus en tunnel hydrodynamique, La Resherche Aeronautique, No. 41, Sep-Oct., 1954, pp. 15-21.

[16] Michell A. M., Molton P., Barberis D. and Delery J., Oscillation of vortex breakdown location and control of the time-averaged location by blowing, AIAA Journal, Vo. 38, No. 5, May 2000, pp. 793-803.

[17] Lambourne, N.C. and Bryer, D.W., The Bursting of Leading Edge Vortices: Some Observation and Discussion of the Phenomenon, Aeronautical Research Council, R&M 3282, 1962.

[18] Lehugeur B. And Gillieron P. and Kourta A. , Experimental investigation on longitudinal vortex control over dihedral bluff body., Exp. Fluids, 48:33-48, 2010.

[19] Smagorinsky J., General circulation experiments with the primitive equations, Monthly Weather Review, Vol. 91, No. 3, pp. 99-165, 1963.

[20] Lehugeur B., Gillieron P. and Ta-Phuoc L., Characterization and control of longitudinal vortices over dihedral bluff body: numerical approach. J Mech Eng 58(5):249-272.

[21] Watanabe M., Harita M. and Hayashi E., The Effect of Body Shapes on Wind Noise, SAE Paper No. 780266, 1978.

[22] Billart P., Chomaz J-M and Huerre P., Experimental study of vortex breakdown in swirling jets, Journal of Fluid Mechanics, Vol. 376, pp: 183-219, 1998.